Engineering Local Polar Frustration in Lead-Free Dielectric Ceramics for Ultrahigh Normalized Energy Storage Performance

ZUBAIRI, Hareem <http://orcid.org/0000-0002-5332-3554>, WASIM, Muhammad <http://orcid.org/0009-0009-0442-068X>, FU, Songhao <http://orcid.org/0009-0002-7708-1841>, LIU, Xiaojiao <http://orcid.org/0000-0003-1989-8407>, KLEPPE, Annette K <http://orcid.org/0000-0002-0258-3241>, LU, Zhilun <http://orcid.org/0000-0002-9967-5221>, FETEIRA, Antonio <http://orcid.org/0000-0001-8151-7009>, XU, Diming <http://orcid.org/0000-0002-7320-0009>, PRENTICE, Joseph C.A. <http://orcid.org/0000-0001-9641-4643> and WANG, Ge <http://orcid.org/0000-0003-1842-8067>

Advanced Functional Materials

ADVANCED FUNCTIONAL MATERIALS
www.afm-journal.de

RESEARCH ARTICLE OPEN ACCESS

Engineering Local Polar Frustration in Lead-Free Dielectric Ceramics for Ultrahigh Normalized Energy Storage Performance

Hareem Zubairi[1] | Muhammad Wasim[2] | Songhao Fu[3] | Xiaojiao Liu[4] | Annette K Kleppe[4] | Zhilun Lu[3] | Antonio Feteira[2] | Diming Xu[5] | Joseph C.A. Prentice[1] | Ge Wang[1]

[1]Department of Materials, University of Manchester, Manchester, UK | [2]School of Engineering and Built Environment, Sheffield Hallam University, Sheffield, UK | [3]School of Chemical and Process Engineering, University of Leeds, Leeds, UK | [4]Diamond Light Source, Harwell Campus, Oxfordshire, UK | [5]Multifunctional Materials and Structures, Key Laboratory of the Ministry of Education & International Centre for Dielectric Research, School of Electronic Science and Engineering, Xi'an Jiaotong University, Xi'an, China

Correspondence: Ge Wang (ge.Wang@manchester.ac.uk)

Received: 17 June 2026 | **Revised:** 31 July 2026 | **Accepted:** 11 August 2026

Keywords: density functional theory | in situ synchrotron XRD | lead-free | normalized energy density | relaxor ferroelectric | thermal stability

ABSTRACT

Lead-free dielectric capacitors require high-recoverable energy density and thermal stability under low operating fields to prevent premature breakdown. Here, we demonstrate a design strategy for high-performance lead-free dielectrics based on two key principles: selecting a highly polarizable ferroelectric matrix and engineering local polar frustration to suppress long-range order and stabilize an ergodic relaxer state. Using the $(0.94Na_{0.5}Bi_{0.5}TiO_3\text{-}0.06BaTiO_3)$–$x(0.85NaNbO_3\text{-}0.15CaTiO_3)$ (NBT-BT-NN-CT) as an exemplar in this work, structural analyses reveal that NN-CT incorporation induces a frustrated polar structure characterized by the nanoscale coexistence of rhombohedral, tetragonal, and cubic-polymorphs. Density functional theory confirms that energetic degeneracy physically prevents the formation of stable macro-domains. The optimal composition yields wide temperature stability (±15% permittivity up to 370°C), far exceeding the X7R industrial standard, delivering a recoverable energy density of >5 J cm^{-3} under low field (250 kV cm^{-1}) achieving an ultrahigh normalized energy density (W_a) of >0.020 mC cm^{-2}, 60% improvement over conventional NBT-based counterparts in the literature (e.g., 0.012–0.015 mC cm^{-2}). Furthermore, in situ synchrotron X-ray diffraction (<160 kV cm^{-1}) provides strong crystallographic evidence of this dynamic structural stability, confirming the absence of irreversible field-induced phase transitions. These results establish polar frustration engineering as a transferable design principle for resilient, high-performance lead-free dielectrics.

1 | Introduction

Achieving net-zero CO_2 emissions by 2050 requires the development of efficient, environmentally friendly technologies capable of harvesting renewable energy resources like wind and solar [1]. To ensure effective generation, conversion, and distribution, all components of the power electronics infrastructure must exhibit high performance, thermal stability, and reliability. Consequently, next-generation systems such as smart grids, hybrid energy systems, and electric vehicles (EVs) require advanced energy storage solutions. Dielectric capacitors are highly attractive for these applications due to their exceptionally high-power density, fast charge/discharge capabilities, long operational lifetimes, and excellent thermal stability [2]. However, conventional high-performance dielectric materials, particularly lead-based ceramics such as $Pb(Zr, Ti)O_3$ (PZT), pose severe environmental

and health risks [2]. This has driven a global mandate (e.g., under RoHS and REACH regulations) to progressively replace them with lead-free alternatives that deliver comparable or superior performance [3].

The core challenge in dielectric capacitor design is maximizing both recoverable energy storage density (W_{rec}) and efficiency (η). The total stored electric energy density (W) for a ceramic dielectric is evaluated by $W = \int_0^{P_{max}} E\, dP$, where E is the applied electric field, and P_{max} is the maximum polarization. The recoverable energy density is obtained by integrating the area between the polarization axis and the discharge curve of the P-E hysteresis loop, calculated as $W_{rec} = \int_{P_r}^{P_{max}} E\, dP$ where P_r is the remnant polarization. The recovery efficiency (η) is therefore defined as $\eta = \frac{W_{rec}}{W} \times 100\%$. Achieving optimal energy storage requires a high P_{max}, a near-zero P_r, a high dielectric breakdown strength (E_b), and consequently, minimal hysteresis loss (W_{loss}). For these reasons, relaxer ferroelectrics (RFEs) offer the most promising balance of properties. Their highly dynamic polar nanoregions (PNRs) provide a strong field-induced polarization while ensuring a slim hysteresis loop upon the charge-discharge mechanism [2].

Most reported lead-free candidates focus on achieving a high recoverable energy density W_{rec} by pushing materials to extreme electric fields (E_{max})>500 kV cm^{-1} [4–6]. However, the equivalent operating voltage (V) is determined by the dielectric layer thickness (t), which is equally important in practical applications. For instance, while ceramic thin films (t < 1 μm) can withstand ultrahigh electric fields (up to 12000 kV cm^{-1}), their operating voltages remain < 50 V [7, 8]. Despite high local energy densities, their minute active dielectric volume severely restricts overall absolute energy storage capacity. Conversely, multilayer ceramic capacitors (MLCCs with t = 1- 20 μm) achieve higher volumetric efficiency under moderate voltages (up to 2000V). For bulk ceramics (t > 100 μm), which provide the highest volumetric energy storage capacity and elevated voltage tolerance required for power grid and electric vehicle infrastructures, pushing E_{max} > 500 kV cm^{-1} leads to applied voltages (>5000 V) [2]. Operating near these conditions poses significant risk to reliability due to electrical and mechanical breakdown and intensified leakage currents. It is therefore critical to maximize the normalized energy density (W_a), defined as $W_a = \frac{W_{rec}}{E_{max}}$, under lower operating electric fields, as one of the primary bottlenecks for unlocking high-performance, structurally resilient bulk dielectrics [2]. To date, conventional lead-free compositions are heavily bottlenecked by this parameter; typical $NaNbO_3$-based systems exhibit W_a values in the modest range of 0.010 mC cm^{-2}, while $BiFeO_3$-based ceramics generally achieve around 0.015 mC cm^{-2} [5, 9–11]. Even state-of-the-art NBT-based systems rarely exceed 0.015 mC cm^{-2} [12–14], whereas high-entropy systems are capable of reaching 0.02 mC cm^{-2} under very high electric fields up to 700 kV cm^{-1} [15].

To design new lead-free dielectric ceramics with a desirable W_a, generating large field-induced polarization under comparably low electric fields is the key to unlocking the materials' full potential. An ideal material should exhibit highly dynamic PNRs to achieve a high P_{max} to drive up W_a, but also the polar correlation length needs to retain a short-range order to suppress hysteresis losses for high η. We achieve this conceptual design by engineering multiple, highly dynamic PNRs into an ergodic relaxer host system through local polar frustration behavior. The design principle begins with the selection of a highly polarizable $Na_{0.5}Bi_{0.5}TiO_3$-0.06$BaTiO_3$ (NBT-6BT) matrix as host [16–18]. NBT-6BT is positioned at the morphotropic phase boundary (MPB), where rhombohedral (R) and tetragonal (T) phases coexist, capable of producing high field-induced P_{max} (>40 μC cm^{-2}) and P_r (>20 μC cm^{-2}) [19]. Nevertheless, it exists as a non-ergodic relaxer at room temperature and undergoes irreversible long-range ferroelectric ordering under applied electric fields (Figure 1a). Consequently, significant macroscopic polarization is retained upon field removal, leading to large hysteresis losses and reduced efficiency [16, 20–23]. To fully achieve the energy storage potential of NBT-6BT, the system must then be transitioned from a non-ergodic to an ergodic relaxer state at room temperature. To disrupt this long-range ferroelectric/non-ergodic relaxer behavior, we introduce the short-range orthorhombic (O) 0.85$NaNbO_3$-0.15$CaTiO_3$ (NNCT) into the host matrix (Figure 1b) [24–26]. In our previous research [27], NNCT was found as a short-range O phase with a high room-temperature permittivity of 2365 and a slim P-E loop. By incorporating NNCT, this precise compositional strategy is intended to suppress long-range R+T ferroelectrics for an ergodic relaxer behavior. Here, we demonstrate this design strategy successfully for optimal normalized energy storage behavior in a quadruple solid solution of NBT-6BT-NN-CT through atomic-resolution high-angle annular dark-field scanning transmission electron microscopy (HAADF-STEM), in situ poling synchrotron X-ray diffraction, crystallo-chemical principles, and density functional theory (DFT). By directly coupling this atomic-scale frustration to macroscopic electrical behavior, the system represents a future direction for providing reliable ultrahigh energy storage performance operating under low electric fields.

2 | Experimental Methods

2.1 | Material Synthesis

The (0.94$Na_{0.5}Bi_{0.5}TiO_3$-0.06$BaTiO_3$)-x(0.85$NaNbO_3$-0.15$CaTiO_3$) ceramics, hereafter denoted as xNNCT (where x = 0.00 to 0.25), were prepared using a conventional solid-state reaction method. Analytical-grade powders of Na_2CO_3 (99.9%, Sigma Aldrich, USA), Bi_2O_3 (99.0%, Merck, Germany), $BaCO_3$ (99.98%, Sigma Aldrich, USA), Nb_2O_5 (99.9%, Sigma Aldrich, China), $CaCO_3$ (99.0%, Sigma Aldrich, Germany), and TiO_2 (99.9%, Sigma Aldrich, Japan) were dried to remove moisture. The precursors were weighed in stoichiometric ratios and ball-milled in propan-2-ol for 24 hours. The dried mixtures were calcined at 900°C for 5 hours to remove volatile impurities and activate the precursors, followed by a second ball-milling step to ensure chemical homogeneity. The resulting powders were mixed with 1 wt.% polyvinyl alcohol (PVA) binder and pressed into 10 mm-diameter ceramic pellets under a uniaxial pressure of 150–180 MPa. Following a binder burnout stage at 550°C for 2 hours, the pellets were sintered at 1160–1180°C with a heating rate of 3°C min^{-1}, yielding dense ceramics with relative densities exceeding 92% measured using 10 samples for each composition (Table S1 and Figure S1).

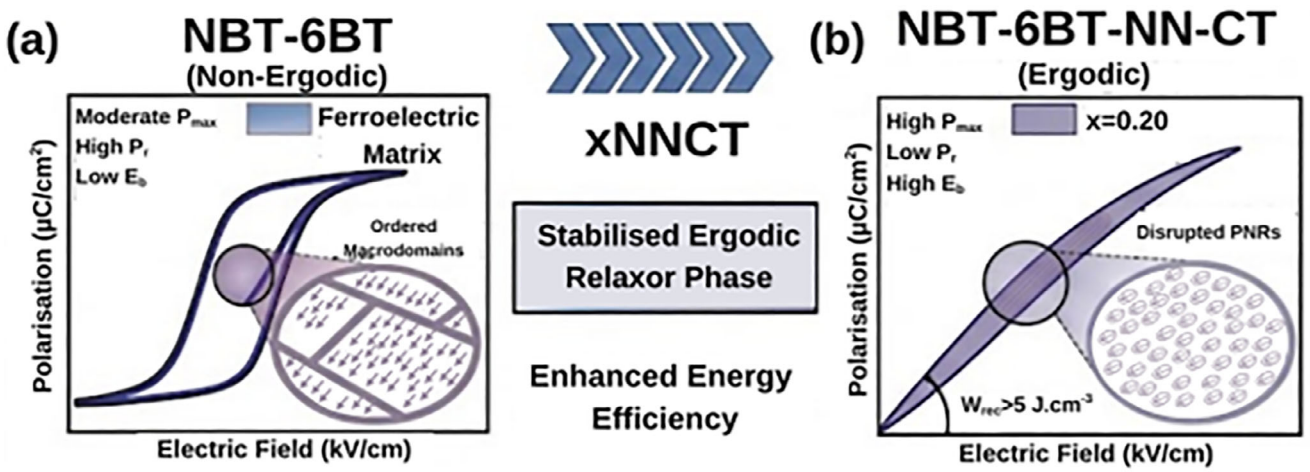

FIGURE 1 | Schematic of the polar frustration engineering strategy. (a) The non-ergodic NBT-6BT host matrix with high P_r and large macrodomains. (b) Introduction of xNNCT disrupts this long-range order, transitioning the material into an ergodic relaxer state, resulting in low P_r and high P_{max} for enhanced energy storage efficiency.

2.2 | Advanced Structural and Electrical Characterization

Microstructural morphology was examined using field-emission scanning electron microscopy (FE-SEM, Quanta 250, FEI, Japan). Before SEM imaging, samples were ground, polished, and thermally etched at 70% of their sintering temperature for 10 minutes. For nanoscale analysis, electron-transparent specimens were prepared using a focused ion beam (FIB, FEI Quanta 3D, The Netherlands) and imaged using an FEI Tecnai G2-20 microscope (The Netherlands). Samples for atomic-scale structural cross-sectional of the (100) and (110) planes were prepared for STEM analysis using a Helios 5 UX (Thermo Fisher Scientific, USA) dual-beam focused ion beam system (FIB) and mounted onto Omniprobe copper-based lift-out grids. Aberration-corrected STEM (AC-STEM) images were acquired with a JEM-ARM300F2 instrument (JEOL, Japan), equipped with a cold field-emission gun operating at 300 kV on a Oneview IS camera, using the high-angle annular dark-field (HAADF-STEM) method, along with atomic-resolution energy-dispersive X-ray spectroscopy (EDS) mapping. The data were processed using the Atomap Python package, including atomic position determination, 2D Gaussian refinement, image analysis, mapping, and polarization vector analysis [28].

To evaluate structural stability under extreme electric fields, in situ poling synchrotron XRD experiments were conducted at the I15 beamline of the Diamond Light Source (72 keV, $\lambda = 0.1722$ Å). Bar-shaped samples with dimensions of $5 \times 1 \times 1$ mm^3 were cut from the ceramic pellets. The samples–detector distance was set to 860 mm, and the detector geometry was precisely calibrated using a standard LaB_6 powder. The incident X-ray beam size at the sample position was 150×120 μm^2. To minimize surface damage and residual stresses induced by machining, the samples were polished and subsequently annealed at 400°C. The specimens were mounted in a polyimide holder filled with silicone oil and connected to a high-voltage amplifier. Diffraction patterns were collected in transmission mode under applied electric fields up to 160 kV cm^{-1} using a Pilatus3 X CdTe 2M detector. The 2D diffraction data were processed and integrated using DAWN [29]. Peak positions, intensities and refinements were analyzed using TOPAS 6 [30].

For electrical measurements, the sintered pellets were polished to a thickness of 0.2 mm and fully electrode with silver paste (area of ≈40 mm^2), followed by firing at 500°C for 30 minutes. Temperature-dependent dielectric properties were recorded from room temperature to 550°C at frequencies of 1, 10, and 100 kHz using an LCR meter (HP 4284A Precision LCR Meter, Agilent Technologies, USA). Polarization-electric field (P-E) hysteresis loops were recorded at 1 Hz in a silicone oil bath using a ferroelectric test system (TF Analyser 2000, aixACCT, Germany).

2.3 | Density Functional Theory (DFT) Calculations

For the first-principles modelling part, it was not computationally feasible to examine the full disordered NBT-BT-NN-CT system. Instead, we considered the parent NBT system. Then we examined the effect of three substitutions: Nb for Ti, Ba for Bi, and Ca for Bi, as a simplified strategy to understand the role of individual chemical species in destabilizing the host matrix. To achieve this, we generated a set of special quasirandom structures (SQS) with the sqsgenerator code [31]. These were structures that were constructed to mimic the correlations of a truly random alloy in a much smaller periodic system. These structures were formed from a $2 \times 2 \times 2$ supercell of a cubic perovskite unit cell, with the pseudo-cubic unit-cell lattice parameter set to the experimental value of 3.9055 Å. Each supercell therefore contained 40 atoms in total. 8 SQS were constructed for each of four compositions: $Na_{0.5}Bi_{0.5}TiO_3$, $Na_{0.5}Bi_{0.5}Ti_{0.875}Nb_{0.125}O_3$, $Na_{0.5}Bi_{0.375}Ba_{0.125}TiO_3$, and $Na_{0.5}Bi_{0.375}Ca_{0.125}TiO_3$. Each of these cubic SQS was then subjected to two volume-conserving distortions: a tetragonal distortion by modifying the c/a ratio, and a rhombohedral distortion by modifying the angle between lattice vectors α. By scanning through possible tetragonal and rhombohedral distortions, optimizing the positions of the atoms for a given set of lattice parameters, and computing the energies of the resulting structures with DFT, we were able to obtain

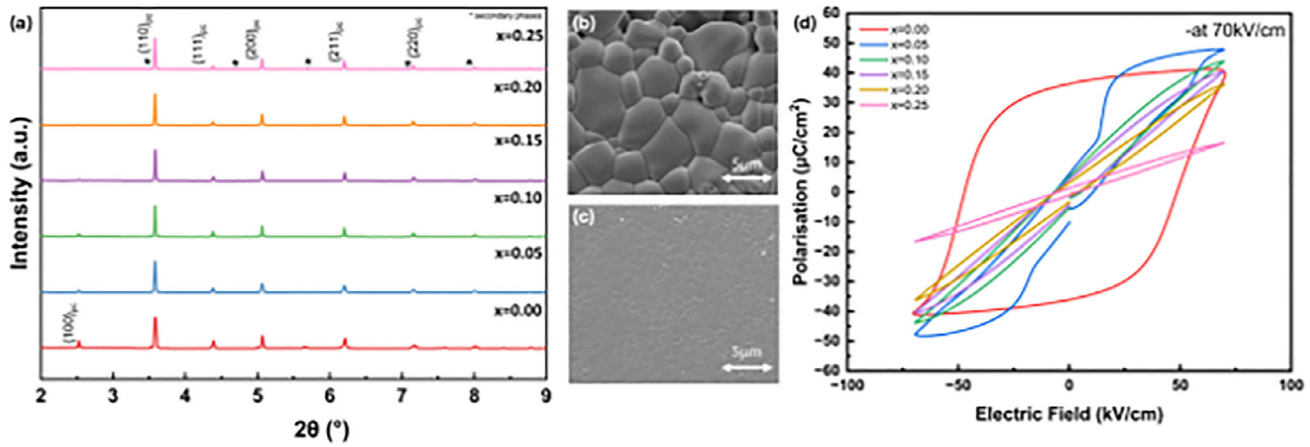

FIGURE 2 | (a) XRD patterns and (b, c) SEM micrographs of x = 0.00 and x = 0.20, and (d) P–E loops at 70 kV cm^{-1} of NBT-6BT-xNNCT ceramics ($0.00 \leq x \leq 0.25$).

the energy of the most stable tetragonal and rhombohedral distortions, alongside the energy of the cubic structure, allowing us to compare them. DFT calculations were carried out using the plane-wave pseudopotential DFT package CASTEP [32]. The PBE functional [33] and CASTEP's on-the-fly-generated (OTFG) ultrasoft pseudopotentials were used for all calculations. A cutoff energy of 600 eV and a 5 × 5 × 5 k-point grid were used throughout. Atomic positions were optimized until the maximum force on an atom was less than 0.1 eV/Å; the electronic energy was converged to within 1×10^{-8} eV.

3 | Results and Discussion

3.1 | Macroscopic Structural and Electrical Performance

The crystallographic and microstructural evolution of the NBT-6BT-xNNCT ceramics (x = 0.00-0.25) as a function of NN-CT content is shown in Figure 2. The NBT-6BT matrix exhibits a mixture of rhombohedral and tetragonal (R+T) phases at the MPB, respectively [34]. However, the addition of the orthorhombic NN-CT modifier progressively merges the split diffraction peaks into a singlet, reflecting enhanced structural disorder and a gradual transition toward a pseudocubic symmetry on average (Figure 2a). However, increasing the dopant to x > 0.20 results in the emergence of secondary phases, indicating a solubility limit within the perovskite lattice. Full-pattern Rietveld refinement on synchrotron X-ray diffraction data with no field on confirms that the x = 0.00 composition is best described by a coexisting Rhombohedral R3c and Tetragonal P4mm model. In contrast, the NN-CT modified compositions are best refined using a single cubic Pm $\bar{3}m$ symmetry (Figure S2). Furthermore, a systematic shift of the (200) reflection to lower 2θ values (Figure S3) indicates an overall lattice expansion, driven by the substitution of smaller Bi^{3+} (1.36 Å) and Ti^{4+} (0.61 Å) host ions with larger Na^{+}/Ca^{2+} (1.38 Å) and Nb^{5+} (0.64 Å) ions from the NN-15%CT dopant [35].

Microstructural analysis via SEM (Figure 2b,c) reveals dense ceramics free of secondary phases (confirmed by EDS mapping, Figure S4). Notably, the average grain size (AGS) is drastically reduced from 3.3 ± 0.12 μm (x = 0.00) to 0.9 ± 0.03 μm (x = 0.20) (Figure S5). This >70% reduction in average grain size (from 3.3 to 0.9 μm) reflects a synergistic optimization between extrinsic microstructural engineering and intrinsic lattice-scale design. Extrinsically, the sub-micron grain size increases the volume fraction of resistive grain boundary interfaces. In accordance with the theoretical dielectric breakdown relation ($E_b \propto G^{-n}$) [36], E_b is enhanced by increasing electrical breakdown pathways and mitigating localized space-charge accumulation [37, 38]. Furthermore, this physical grain confinement actively promotes the disruption of macroscopic, long-range ferroelectric domains, favoring the formation of short-range polar structures [39]. Intrinsically, however, microstructural confinement alone typically decreases P_{max} in conventional ferroelectric ceramics due to the grain boundary clamping effect [40]. The key driver for the record-high normalized energy density W_a > 0.020 mC cm^{-2} happens intrinsically within the grain, more precisely at the crystal lattice level. Here, compositional disorder within the perovskite lattice creates atomic-scale polar frustration, forming coexistence of R, T, and C polymorphs inside the grains, enabling a massive field-induced P_{max} > 55 μC cm^{-2} under low electric fields. Thus, extrinsic grain boundary refinement and intrinsic grain (lattice) polar frustration act synergistically to deliver ultrahigh normalized energy storage performance [41]. The bipolar polarization-electric field (P-E) hysteresis loops of all compositions were evaluated under 70 kV cm^{-1} (Figure 2d). The NBT-6BT composition exhibits a well-saturated, square ferroelectric hysteresis loop with P_{max} = 40 μC cm^{-2} and P_r = 36 μC cm^{-2}, typical of a long-range ferroelectric state [41–43]. However, as the NNCT content increases up to 0.20, the loops become progressively slimmer and more linear, as evidenced by a reduction in P_r toward 3 μC cm^{-2} with P_{max} = 33 μC cm^{-2} at 70 kV cm^{-1}, reflecting the complete suppression of long-range ferroelectricity and the emergence of a highly reversible ergodic relaxer state [42, 44]. The retained high P_{max} is associated with the highly polarizable NBT-6BT host matrix, while the introduction of NN-15%CT promotes a more short-range relaxer behavior. However, at x = 0.25, the emergence of parasitic secondary phases and a significant drop in the P_{max}, limiting the polarizability and acting as the defining upper compositional bound for optimized energy storage in the system.

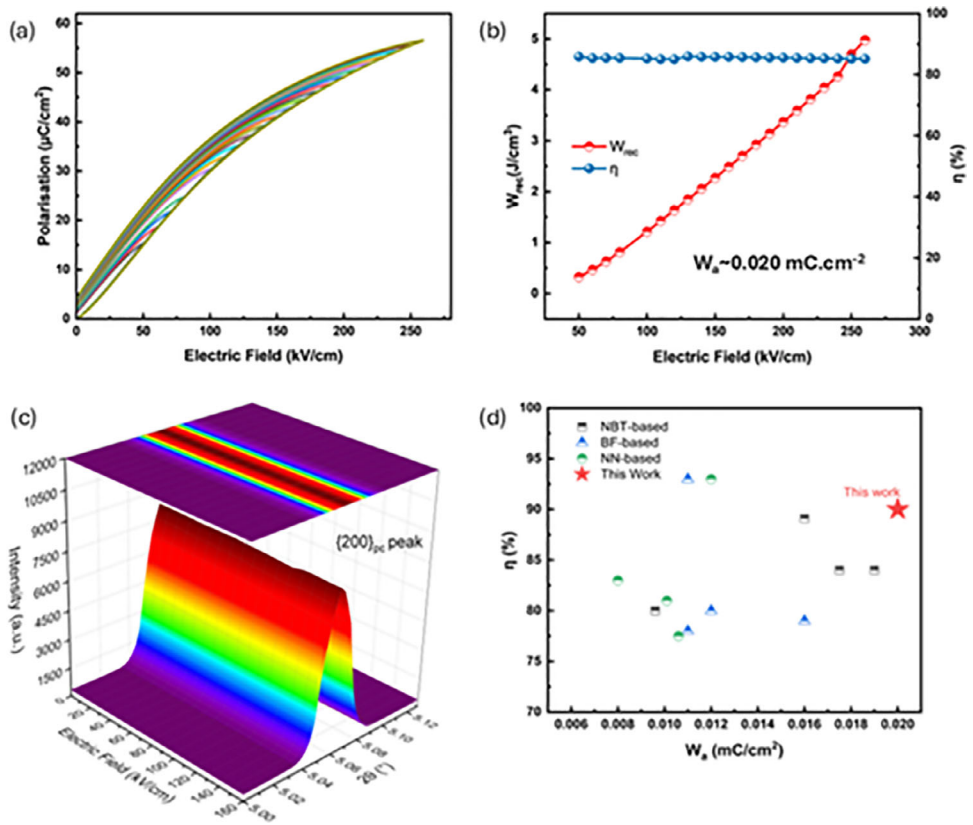

FIGURE 3 | (a) Electric-field-dependent P–E loops up to breakdown strength. (b) Corresponding recoverable energy density (W_{rec}) and efficiency (η) as a function of field. (c) 3D contour plots of the $\{200\}_{pc}$ reflections of in situ synchrotron XRD under applied electric fields, showing no detectable peak splitting, shift, or intensity change, confirming the absence of field-induced phase transitions and the persistence of pseudocubic symmetry under ultrahigh fields of 0.20NNCT ceramics. (d) Comparison of existing literature with the xNNCT ceramics.

The optimal composition is found at x = 0.20 with a high P_{max} > 55 μC cm^{-2}, P_r < 4 μC cm^{-2} derived from unipolar P–E loops measured at a field of ≈250 kV cm^{-1}, resulting in a W_{rec} > 5 J cm^{-3} and an η of > 85% (Figure 3a,b and Figure S6). Notably, such a high P_{max} is achieved under comparatively low electric fields [15], while the origin of the enhanced polarizability and its field stability will be further elucidated later through advanced structural characterization and DFT analysis. The normalized energy density (W_a) reveals a record-high W_a of 0.02 mC cm^{-2} (at low field <250 kV cm^{-1}) among all other reported lead-free candidates (Figure 3d and Table S2) [2]. This value, coupled with high η, places the current material at the forefront of the reported literature. Furthermore, the relationship between W_a and polarization change (ΔP = 0.052 mC cm^{-2}) follows the established linear trend (W_a = k. ΔP) with a slope k < 0.5 [2]. This confirms that the record W_a primarily originates from the substantial increase in ΔP while retaining the ideal relaxer P-E profile characteristics.

To evaluate the structural stability under high field, in-situ poling synchrotron X-ray diffraction was performed on the optimized composition with x = 0.20 ceramic under applied electric fields up to 160 kV cm^{-1}. Under the application of an electric field at 5 kV cm^{-1} increments up to 160 kV cm^{-1}, the representative peaks (111), (200), and (220) reflections remain singlet and exhibit no detectable peak split, shift or macroscopic intensity redistribution (Figure 3c and Figure S7). The corresponding full width at half maximum (FWHM) obtained from pseudo-Voigt profile fitting was also found to be relatively stable with negligible variations, Figure S8. In most of the reported NBT-based materials for piezoelectric applications, those features are the classical crystallographic signatures of a field-induced phase transition (e.g., an irreversible ferroelectric-to-relaxer transformation), which destabilizes the ergodic relaxer state, and theoretically promotes hysteresis losses and significant drops in the energy conversion efficiency [45]. The absence of long-range orders in our study confirms that the pseudocubic relaxer state persists even under high electrical loading [46].

3.2 | Thermal Stability Behavior

Thermally induced dielectric properties are an important feature for a capacitor, as key to operate and maintain functional reliability. Temperature-dependent dielectric permittivity (ε_r) and loss (tanδ) measured at 1–100 kHz (Figure 4a and Figure S9) reveal a systematic broadening and a shift of the permittivity maximum (T_m) toward lower temperatures. The room-temperature tanδ decreases dramatically with NN-CT doping from 0.10 at x = 0.00 to 0.02 at x = 0.20 at 1 kHz. The dielectric loss for x = 0.20 exhibits frequency dispersion more obviously, indicating the strong relaxer nature of the compositions [47]. The dielectric loss increases abruptly above 250°C at 1 kHz, probably due to the thermally activated mobile oxygen vacancies and

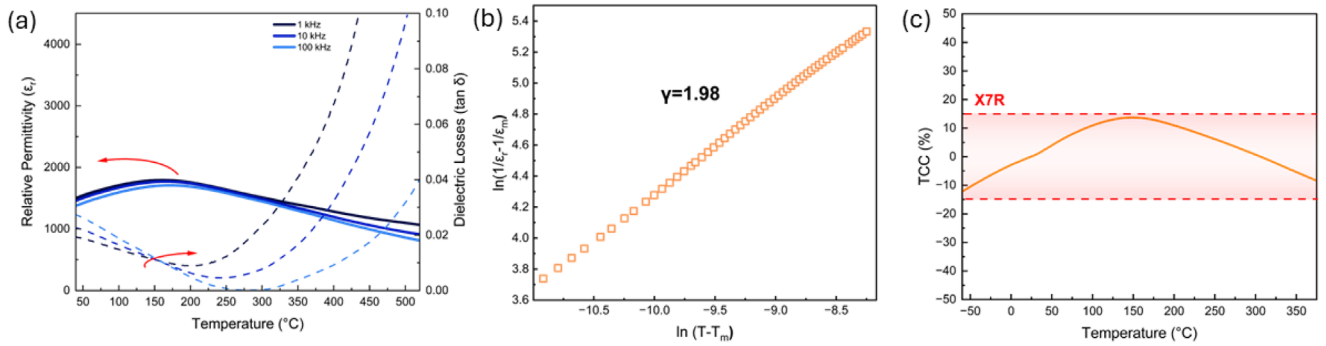

FIGURE 4 | (a) Frequency-dependent permittivity (ε_r) and dielectric loss (tan δ) at 1–100 kHz (b) Modified Curie–Weiss plots indicating relaxer behavior (c) Temperature coefficient of capacitance (TCC) within ±15% up to 370°C, exceeding the X7R standard of 0.20NNCT ceramics.

space-charge conduction. This significant increase indicates a change in the conduction mechanism and suggests that the operating temperature of this ceramic composition should not exceed approx. 300°C, where tan$\delta \approx 0.025$ [48]. Furthermore, the degree of diffuseness (γ), extracted from the modified Curie-Weiss law (Lorentzian relation) (Figure 4b and Figure S10), increases systematically with NN-CT towards 2 (the ideal relaxer limit) [49]. From an application perspective, the thermal stability of x = 0.20 is exceptional, exhibiting a highly stable permittivity with Temperature Coefficient of Capacitance (TCC) ±15% up to 370°C (measured at 1 kHz) (Figure 4c), far exceeding the upper limit of the commercial X7R capacitor standard (125°C) [50].

3.3 | Local Structural and Thermodynamic Origin of Nanoscale Polar Frustration

To further reveal the origin of the high energy density of optimal composition, advanced microscopy (local structure), coupled with a thermodynamic (phase formation) approach, was employed. Local structural behavior of the optimized composition, x = 0.20, is characterized by a dark-field image under TEM coupled with selected-area electron diffraction (SAED), shown in Figure 5a. SAED patterns along the <111> and <110> zone axes (Figure 5a insets 1–2) display diffuse scattering and weak ½(ooe) and ½ <ooo> superlattice reflections [51]. These features are indicative of short-range correlated displacements and dynamic octahedral tilting, directly contrasting with long-range order reported in NBT-6BT [13]. Specifically, the <111> zone highlights typical local rhombohedral distortions, whereas the <110> zone emphasizes the absence of long-range octahedral tilt order, collectively verifying the intrinsically pseudocubic character of the phase [38]. To further investigate the nanoscale behavior underlying this pseudocubic average symmetry, high-angle annular dark-field scanning transmission electron microscopy (HAADF-STEM) imaging was performed on the x = 0.20, shown in Figure 5b. Polarization vector mapping, which was determined from the displacements of B-site cations relative to the centers of their four nearest A-site neighbors, reveals a highly complex, frustrated polar structure. In these maps, arrow lengths represent the magnitude of the atomic displacements, while orientations indicate the local polarization direction. Vectors aligned close to the $[001]_c$ axis were classified as tetragonal-like (T), those along $[011]_c$ as rhombohedral/orthorhombic-like (R/O), and negligible displacements as cubic-like (C) [15, 52, 53]. Enlarged views (Figure 5c–e) dramatically highlight representative T, R, and C regions coexisting at the nanoscale. These distinct structural regions are only a few nanometers in size, significantly smaller than conventional ferroelectric macro-domains, thereby confirming their nature as dynamic PNRs. This nanoscale heterogeneity underlies the pseudocubic average symmetry observed via synchrotron x-ray diffraction. Finally, the schematic order–disorder map (inset in Figure 5b) summarizes this unique structural scenario: locally correlated T and R polar regions embedded within a largely disordered C matrix.

This interpretation is additionally supported by DFT calculations of the energy difference between R, T, and C states as Nb, Ba, and Ca are each introduced into the lattice. It is important to note that DFT is a zero-temperature (0K) theory, so these results should be interpreted in that light. For example, in common with many perovskites, the cubic structure is not the structure with the lowest energy here (although it may be the structure with the lowest free energy, once vibrational and other entropic contributions are considered). These contributions could in theory be considered, but to do so for all configurations considered here, at an acceptable degree of accuracy, would be computationally impractical. However, DFT energy differences between cubic, tetragonal, and rhombohedral structures can still provide information about the relative stability of these structures, and therefore insight into potential structural changes. These calculated energy differences are shown in Figure 5f, with examples of the different structures shown in Figure 5g.

In the parent material, NBT, the lowest energy structure is invariably predicted to be T, usually by some margin. When other elements are added, the energy differences between T, R, and C become smaller, and the lowest energy structure becomes much more variable. R structures become more competitive, but the precise ordering of the structures depends strongly on the exact environment in the SQS. This suggests that a variety of different states are energetically competitive depending on the local composition and environment, resulting in these states coexisting through the material, as seen experimentally. Collectively, these complementary techniques establish that NNCT (20%) incorporation drives the system towards a pseudocubic average structure while stabilizing nanoscale heterogeneity, thus providing the structural foundation for the ergodic relaxer behavior.

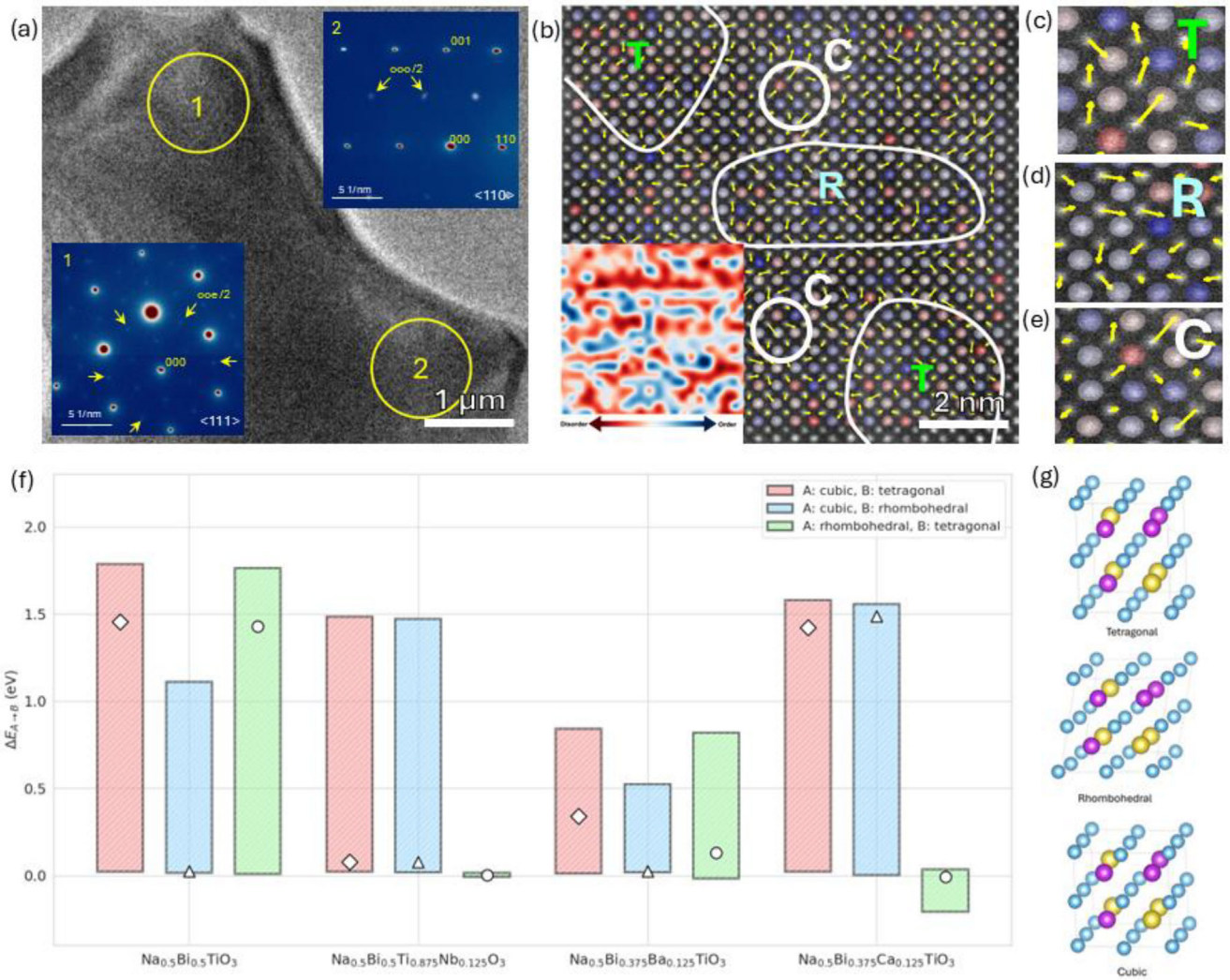

FIGURE 5 | (a) Dark Field TEM image for 0.20NNCT showing local disorder. (1, 2 insets) SAED patterns along <111> and <110> zone axes displaying diffuse scattering. (b) Atomic-resolution HAADF-STEM image of x = 0.20 with polarization vector mapping derived from B-site displacements, showing coexisting tetragonal (T), rhombohedral (R), and cubic-like (C) nanoregions; (Inset showing polarization disorder (red) – order (blue) mapping highlighting nanoscale heterogeneity and short-range correlations) (c–e) enlarged views of representative T, R, and C regions. (f) Energy differences between cubic, tetragonal, and rhombohedral structures, as computed with DFT for a set of 8 SQS for each composition. Shapes mark the median value of $\Delta E_{A\rightarrow B}$ over all 8 SQS; the lines show the range of $\Delta E_{A\rightarrow B}$ values produced. A positive (negative) value for $\Delta E_{A\rightarrow B}$ means that structure B is lower (higher) in energy than structure A. (g) Example periodic unit cells used in the DFT calculations, showing the cubic structure and the two different distortions applied. The distortions have been deliberately exaggerated for visualization purposes. The cells shown are for a particular SQS representing $Na_{0.5}Bi_{0.5}TiO_3$. Na, Bi, and Ti are shown in yellow, purple, and blue, respectively; O atoms are not shown for clarity.

4 | Conclusions

In summary, we have successfully developed a highly robust, lead-free dielectric capacitor material by systematically engineering an ergodic relaxer state via local polar frustration. By introducing the chemically disordered NN-CT modifier into a highly polarizable NBT-6BT matrix, we effectively suppressed long-range ferroelectric order. Validated by atomic-scale HAADF-STEM imaging and DFT, we demonstrated that a frustrated polar landscape drives this structural evolution. This energetic degeneracy enables the nanoscale coexistence of rhombohedral, tetragonal, and cubic polymorphs, providing a highly dynamic pseudocubic matrix that easily polarizes under an applied field but resists macroscopic domain formation. This precise atomic-scale structural control directly translates into outstanding macroscopic energy storage performance. The optimized composition (x = 0.20) achieves a highly reversible, slim polarization response, yielding a remarkable normalized W_a of >0.02 mC cm^{-2} with η>85%. Furthermore, the system also exhibits exceptional thermal stability with a stable TCC up to 370°C, far exceeding the X7R industrial standard. Crucially, in-situ synchrotron X-ray diffraction provides definitive crystallographic proof that this pseudocubic ergodic relaxer state is retained with negligible phase transitions even under extreme electric fields up to 160 kV cm^{-1}. Overall, this study establishes a fundamental, atomic-to-macroscopic design paradigm. By coupling thermodynamic free-energy flattening with nanoscale structural frustration, we provide a generalizable strategy for the development of future lead-free dielectric ceramics, thereby accelerating their integration into

next-generation power electronics and sustainable energy storage systems.

Author Contributions

Hareem Zubairi: Writing:- original draft, investigation, methodology, data curation, formal analysis, conceptualization. **Muhammad Wasim**, **Songhao Fu**, **Xiaojiao Liu**, **Annette K Kleppe**, **Zhilun Lu**, **Antonio Feteira**, **Diming Xu**, **Joseph C.A. Prentice** Data curation. **Ge Wang**: Writing – review & editing, supervision, validation, conceptualization, investigation.

Acknowledgements

The authors gratefully acknowledge the financial support from the Dean's PhD Scholarship by the University of Manchester and the Dame Kathleen Ollerenshaw Fellowship. Also, MW gratefully acknowledges the financial support provided through the PhD Graduate Teaching Assistantship (GTA) scholarship scheme at Sheffield Hallam University, UK. The authors would also like to acknowledge the support of Diamond Light Source (proposal no CY39563-1) for accessing the synchrotron experiment.

Conflicts of Interest

The authors declare no conflicts of interest.

Data Availability Statement

The data that support the findings of this study are available from the corresponding author upon reasonable request.

References

1. M. H. Zhang, L. Fulanović, C. Zhao, and J. Koruza, "Review on Field-induced Phase Transitions in Lead-free $NaNbO_3$-based Antiferroelectric Perovskite Oxides for Energy Storage," *Journal of Materiomics* 9 (2023): 1–18, https://doi.org/10.1016/J.JMAT.2022.09.008.

2. H. Zubairi, Z. Lu, Y. Zhu, and I. M. Reaney, and G. Wang, "Current Development, Optimisation Strategies and Future Perspectives for Lead-free Dielectric Ceramics in High Field and High Energy Density Capacitors," *Chemical Society Reviews* 53 (2024): 10761–10790, https://doi.org/10.1039/D4CS00536H.

3. H. Tao,, H. Wu, Y. Liu, et al., "Ultrahigh Performance in Lead-Free Piezoceramics Utilizing a Relaxor Slush Polar State with Multiphase Coexistence," *Journal of the American Chemical Society* 141 (2019): 13987–13994, https://doi.org/10.1021/JACS.9B07188/ASSET/IMAGES/LARGE/JA9B07188_0005.JPEG.

4. H. Qi, R. Zuo, A. Xie, et al., "Ultrahigh Energy-Storage Density in $NaNbO_3$ -Based Lead-Free Relaxor Antiferroelectric Ceramics with Nanoscale Domains," *Advanced Functional Materials* 29 (2019): 1903877–1903877, https://doi.org/10.1002/ADFM.201903877.

5. W. Zhu, Y. Ji, C. Cheng, et al., "High and Stable Energy-storage Performance in $BiFeO_3$ Ceramics via High-entropy Design," *Journal of Energy Storage* 159 (2026): 121867, https://doi.org/10.1016/j.est.2026.121867.

6. Y. Tao, H. Yang, M. Wang, B. Zheng, and Y. Lin, "High Energy Storage Efficiency and Exceptional Recoverable Energy Storage Density Achieved in KNN-based Ceramics via Entropy Engineering," *Journal of Alloys and Compounds* 1024 (2025): 180210, https://doi.org/10.1016/j.jallcom.2025.180210.

7. W. Dong, C. Magén, J. Zou, et al., "Leveraging the Integration of Perovskite $BaTiO_3$ on Ferroelectric Fluorite HfO_2 to Enhance Energy Storage Cyclability and Efficiency," *Nano Energy* 151 (2026): 111810, https://doi.org/10.1016/j.nanoen.2026.111810.

8. L. Zhang, R. Jing, S. Zhang, and L. Jin, "Multiscale Microstructure Design for High-performance Dielectric Energy Storage Materials," *Microstructures* 6 (2026): 2026003, https://doi.org/10.20517/microstructures.2025.89.

9. L. Lv, Y. Yang, M. Shi, et al., "Dynamic Heterogeneous Nano-microregions for High Energy Storage in $NaNbO_3$-based Ceramics," *Chemical Engineering Journal* 522 (2025): 167790, https://doi.org/10.1016/j.cej.2025.167790.

10. P. Nong, D. Zeng, Y. Pan, et al., "Simultaneous Enhancement of Energy Storage Performance and Thermal Stability of $NaNbO_3$-based Ceramics via Multi-scale Modulation," *Journal of Materiomics* 10 (2024): 670–681, https://doi.org/10.1016/j.jmat.2023.09.004.

11. X. Zhai, M. Lu, J. Du, et al., "Improved Energy Storage Performance in $NaNbO_3$-based Ceramics via Synergetic Phase Regulation and Enhanced Relaxation," *Journal of the European Ceramic Society* 45 (2025): 117151, https://doi.org/10.1016/j.jeurceramsoc.2024.117151.

12. H. Liu, Z. Sun, J. Zhang, et al., "Local Chemical Clustering Enabled Ultrahigh Capacitive Energy Storage in Pb-Free Relaxors," *Journal of the American Chemical Society* 145 (2023): 19396–19404, https://doi.org/10.1021/jacs.3c06912.

13. H. Ji, D. Wang, W. Bao, et al., "Ultrahigh Energy Density in Short-range Tilted NBT-based Lead-free Multilayer Ceramic Capacitors by Nanodomain Percolation," *Energy Storage Materials* 38 (2021): 113–120, https://doi.org/10.1016/j.ensm.2021.01.023.

14. Y. Gao, X. Zhu, B. Yang, et al., "Grain Size Modulated $(Na_{0.5}Bi_{0.5})_{0.65}Sr_{0.35}TiO_3$-based Ceramics with Enhanced Energy Storage Properties," *Chemical Engineering Journal* 433 (2022): 133584, https://doi.org/10.1016/j.cej.2021.133584.

15. W. Cao, Y. Wu, X. Yang, et al., "Breaking Polarization-breakdown Strength Paradox for Ultrahigh Energy Storage Density in NBT-based Ceramics," *Nature Communications* 16 (2025): 6228, https://doi.org/10.1038/s41467-025-61030-7.

16. W. Cao, et al., "Outstanding Energy Storage Performance of NBT-Based Ceramics under Moderate Electric Field Achieved via Antiferroelectric Engineering," *ACS Applied Materials and Interfaces* 15 (2023): 38633–38643, https://doi.org/10.1021/ACSAMI.3C08791/ASSET/IMAGES/LARGE/AM3C08791_0010.JPEG.

17. W. Cao, R. Lin, X. Hou, et al., "Interfacial Polarization Restriction for Ultrahigh Energy-Storage Density in Lead-Free Ceramics," *Advanced Functional Materials* 33 (2023): 2301027–2301027, https://doi.org/10.1002/ADFM.202301027.

18. W. P. Cao, W. L. Li, D. Xu, Y. F. Hou, W. Wang, and W. D. Fei, "Enhanced Electrocaloric Effect in Lead-free NBT-based Ceramics," *Ceramics International* 40 (2014): 9273–9278, https://doi.org/10.1016/j.ceramint.2014.01.149.

19. O. Elkechai, M. Manier, and J. P. Mercurio, "$Na_{0.5}Bi_{0.5}TiO_3$–$K_{0.5}Bi_{0.5}TiO_3$ (NBT-KBT) system: A Structural and Electrical Study," *Physica Status Solidi (A)* 157 (1996): 499–506, https://doi.org/10.1002/pssa.2211570234.

20. R. Zhao, Y. Zhang, W. Li, et al., "Energy Storage and Charge/Discharge Performance of Sm-Doped NBT-Based Lead-Free Ceramics," *ACS Applied Electronic Materials* 5 (2023): 6104–6113, https://doi.org/10.1021/ACSAELM.3C01066.

21. A. Zhang, T. Wang, J. Liu, et al., "Significant Improvement in Energy Storage for BT Ceramics via NBT Composition Regulation," *Journal of Alloys and Compounds* 968 (2023): 172255–172255, https://doi.org/10.1016/J.JALLCOM.2023.172255.

22. H. Li, S. Zhou, J. Zhao, et al., "Dielectric Temperature Stability and Energy Storage Performance of NBT-based Lead-free Ceramics for Y9P Capacitors," *Journal of Advanced Dielectrics* 13 (2023): 2242007–2242007, https://doi.org/10.1142/S2010135x22420073.

23. Y.-S. Zhang, W.-H. Li, X.-G. Tang, et al., "Energy Storage and Charge-discharge Performance of B-site Doped NBT-based Lead-free Ceramics," *Journal of Alloys and Compounds* 911 (2022): 165074–165074, https://doi.org/10.1016/J.JALLCOM.2022.165074.

24. P. Nong, Y. Pan, Q. Dong et al., "Inner Mechanism of Enhanced Energy Storage Properties and Efficiency for $CaTiO_3$ Modified $_{0.92}NaNbO_{3\text{-}0.08}Bi(Mg_{0.5}Ti_{0.5})O_3$ Lead-Free Ceramics," *Electronic Materials Letters* 20 (2024): 1–13, https://doi.org/10.1007/s13391-023-00434-3.

25. A. Xie, J. Fu, R. Zuo, et al., "$NaNbO_3$-$CaTiO_3$ lead-free Relaxor Antiferroelectric Ceramics Featuring Giant Energy Density, High Energy Efficiency and Power Density," *Chemical Engineering Journal* 429 (2022): 132534–132534, https://doi.org/10.1016/J.CEJ.2021.132534.

26. M. Xu, X. Wang, P. Nong, et al., "$Bi(Ni_{0.5}Zr_{0.5})O_3)_{\text{-}0.10}CaTiO_3$ Lead-Free Dielectric Ceramics with High Energy Storage Properties," *ACS Applied Energy Materials* 6 (2023): 1630–1638, https://doi.org/10.1021/ACSAEM.2C03520/SUPPL_FILE/AE2C03520_SI_001.PDF.

27. H. Zubairi, M. Wasim, Y. Liu, et al., "High Permittivity Short-range Orthorhombic Q Phase in $CaTiO_3$ Modified $NaNbO_3$ Ceramics," *Ceramics International* 51 (2025): 59862–59867, https://doi.org/10.1016/j.ceramint.2025.10.204.

28. M. Nord, P. E. Vullum, I. MacLaren, T. Tybell, and R. Holmestad, "Atomap: A New Software Tool for the Automated Analysis of Atomic Resolution Images Using Two-dimensional Gaussian Fitting," *Advanced Structural and Chemical Imaging* 3 (2017): 9, https://doi.org/10.1186/s40679-017-0042-5.

29. M. Basham, J. Filik, M. T. Wharmby, et al., "Data Analysis WorkbeNch (DAWN)," *Journal of Synchrotron Radiation* 22 (2015): 853–858.

30. A. Coelho, "TOPAS and TOPAS-Academic: An Optimization Program Integrating Computer Algebra and Crystallographic Objects Written in C^{++}," *Journal of Applied Crystallography* 51 (2018): 210–218.

31. D. Gehringer, M. Friák, and D. Holec, "Models of Configurationally-complex Alloys Made Simple," *Computer physics communications* 286 (2023): 108664, https://doi.org/10.1016/j.cpc.2023.108664.

32. S. J. Clark, M. D. Segall, C. J. Pickard, et al., "First Principles Methods Using CASTEP," *Zeitschrift für kristallographie* 220(2005): 567–570, https://doi.org/10.1524/zkri.220.5.567.65075.

33. J. P. Perdew, K. Burke, and M. Ernzerhof, "Generalized Gradient Approximation Made Simple," *Physical Review Letters* 77 (1996): 3865–3868, https://doi.org/10.1103/PhysRevLett.77.3865.

34. J. E. Daniels, W. Jo, J. Rödel, and J. L. Jones, "Electric-field-induced Phase Transformation at a Lead-free Morphotropic Phase Boundary: Case Study in a 93%$(Bi_{0.5}Na_{0.5})TiO_3$–7% $BaTiO_3$ Piezoelectric Ceramic$(Bi_{0.5}Na_{0.5})TiO_3$–7% $BaTiO_3$ Piezoelectric Ceramic," *Applied Physics Letters* 95 (2009): 032904, https://doi.org/10.1063/1.3182679.

35. R. D. Shannon and C. T. Prewitt, "Effective Ionic Radii in Oxides and Fluorides," *Acta Crystallographica Section B Structural Crystallography and Crystal Chemistry* 25 (1969): 925–946.

36. C. A. Randall, A. S. Bhalla, T. R. Shrout, and L. E. Cross, "Classification and Consequences of Complex Lead Perovskite Ferroelectrics with Regard to B-site Cation Order," *Journal of Materials Research* 5 (1990): 829–834, https://doi.org/10.1557/JMR.1990.0829.

37. L. Yan, X. Rui, G. Chen, W. Xu, G. Zou, and H. Luo, "Recent Advances in Nanostructured Nb-based Oxides for Electrochemical Energy Storage," *Nanoscale* 8 (2016): 8443–8465, https://doi.org/10.1039/C6NR01340F.

38. T. Wei, J. Zou, X. Zhou, et al., "High-entropy Assisted Capacitive Energy Storage in Relaxor Ferroelectrics by Chemical Short-range Order," *Nature Communications* 16 (2025): 807, https://doi.org/10.1038/s41467-025-56181-6.

39. A. Young, G. Hilmas, S. C. Zhang, and R. W. Schwartz, "Effect of Liquid-Phase Sintering on the Breakdown Strength of Barium Titanate," *Journal of the American Ceramic Society* 90 (2007): 1504–1510, https://doi.org/10.1111/j.1551-2916.2007.01637.x.

40. T. Ogawa, "Poling Field Dependence of Ferroelectric Properties in Barium Titanate Ceramics," *Japanese Journal of Applied Physics* 40 (2001): 5630.

41. Z. Pan, D. Hu, Y. Zhang, J. Liu, B. Shen, and J. Zhai, "Achieving High Discharge Energy Density and Efficiency with NBT-based Ceramics for Application in Capacitors," *Journal of Materials Chemistry C* 7 (2019): 4072–4078, https://doi.org/10.1039/C9TC00087A.

42. J. Lv, Q. Li, Y. Li, et al., "Significantly Improved Energy Storage Performance of NBT-BT Based Ceramics through Domain Control and Preparation Optimization," *Chemical Engineering Journal* 420 (2021): 129900, https://doi.org/10.1016/j.cej.2021.129900.

43. B. Zheng, Y. Lin, H. Yang, et al., "A Broad-High Temperature Ceramic Capacitor with Local Polymorphic Heterogeneous Structures," *Advanced Science* 12 (2025): 2409814, https://doi.org/10.1002/advs.202409814.

44. J. Li, Z. Shen, X. Chen, et al., "Grain-orientation-engineered Multilayer Ceramic Capacitors for Energy Storage Applications," *Nature materials* 19 (2020): 999–1005, https://doi.org/10.1038/S41563-020-0704-X.

45. J. Ji, C. Tian, H. Tang, et al., "Achieve High Dielectric Energy Storage Efficiency and Good Temperature Stability within a Wide Range by High-entropy Induced Relaxor Enhancement Strategy in NBT-based Ceramics," *Chemical Engineering Journal* 522 (2025): 167823, https://doi.org/10.1016/j.cej.2025.167823.

46. Y. Jia, Y. Fan, L. Lei, et al., "In Situ Synchrotron X-ray Diffraction for Actuation in Sodium Bismuth Titanate Relaxor Ferroelectrics," *Materials Horizons* 12 (2025): 5194–5203, https://doi.org/10.1039/D5MH00388A.

47. A. Zeb, S. Jan, F. Bamiduro, D. Hall, and S. Milne, "Temperature-Stable Dielectric Ceramics Based on $Na_{0.5}Bi_{0.5}TiO_3$," *Journal of the European Ceramic Society* (2017): 1548–1555, https://doi.org/10.1016/j.jeurceramsoc.2017.12.032.

48. Z. Wang, L. Zhang, R. Kang, et al., "High Temperature Dielectric Stable $_{(1\text{-}x)}[(Na_{0.5}Bi_{0.5})_{0.92}Ba_{0.08}]_{0.955}La_{0.03}TiO_{3\text{-}x}NaNbO_3$ System with Ultra-low Dielectric Loss Range through Optimizing the Defect Chemistry," *Journal of Alloys and Compounds* 846 (2020): 156308, https://doi.org/10.1016/j.jallcom.2020.156308.

49. J. Hui, Y. Yan, L. Wang, et al., "Improving Energy Storage Properties of NN-NBT Ceramics through Compositional Modification," *Journal of Alloys and Compounds* 989 (2024): 174276, https://doi.org/10.1016/j.jallcom.2024.174276.

50. L. Zhang, Y. Pu, M. Chen, T. Wei, and X. Peng, "Novel $Na_{0.5}Bi_{0.5}TiO_3$ Based, Lead-free Energy Storage Ceramics with High Power and Energy Density and Excellent High-temperature Stability," *Chemical Engineering Journal* 383 (2020): 123154–123154, https://doi.org/10.1016/J.CEJ.2019.123154.

51. Z. Wang, D. Li, W. Liu, et al., "Ultra-high Energy Storage in Lead-free $NaNbO_3$-based Relaxor Ceramics with Directional Slush-like Polar Structures Design," *Nature Communications* 16 (2025): 2892, https://doi.org/10.1038/s41467-025-58268-6.

52. D. Li, Z. Zheng, B. Yang, et al., "Atomic-Scale High-Entropy Design for Superior Capacitive Energy Storage Performance in Lead-Free Ceramics," *Advanced Materials* 37 (2025): 2409639, https://doi.org/10.1002/adma.202409639.

53. S. Zhou, Y. Zhou, L. Li, et al., "Ultrawide-temperature-stable High-entropy Relaxor Ferroelectrics for Energy-efficient Capacitors," *Nature Communications* 16 (2025): 8456, https://doi.org/10.1038/s41467-025-63173-z.

Supporting Information

Additional supporting information can be found online in the Supporting Information section.

Supporting File: adfm77848-sup-0001-SuppMat.docx.